The TopHat experiment: A balloon-borne instrument for mapping millimeter and submillimeter emission

Silverberg, R.F.; Cheng, E.S.; Aguirre, J.E.; Bezaire, J.J.; Crawford, T.M.; Meyer, S.S.; Bier, A.; Campano, B.; Chen, T.C.; Cottingham, D.A.

Total number of authors:
19

Published in:
Astrophysical Journal Supplement Series

Publication date:
2005

Document Version
Publisher's PDF, also known as Version of record

The Astrophysical Journal Supplement Series, 160:59–75, 2005 September

THE TOPHAT EXPERIMENT: A BALLOON-BORNE INSTRUMENT FOR MAPPING MILLIMETER AND SUBMILLIMETER EMISSION

R. F. Silverberg and E. S. Cheng[1]
Laboratory for Astronomy and Solar Physics, NASA Goddard Space Flight Center, Greenbelt, MD 20771

J. E. Aguirre,[2] J. J. Bezaire, T. M. Crawford, and S. S. Meyer
Enrico Fermi Institute, University of Chicago, Chicago, IL 60637

A. Bier, B. Campano, T. C. Chen, D. A. Cottingham, and E. H. Sharp
GST, NASA Goddard Space Flight Center, Greenbelt, MD 20771

P. R. Christensen
Niels Bohr Institute, Copenhagen University, Copenhagen, Denmark

S. Cordone and P. T. Timbie
Department of Physics, University of Wisconsin, Madison, WI 53706

R. E. Dame
Mega Engineering, Silver Spring, MD 20901

D. J. Fixsen
SSAI, NASA Goddard Space Flight Center, Greenbelt, MD 20771

R. J. K. Kristensen and H. U. Nørgaard-Nielsen
Danish Space Research Institute, Copenhagen, Denmark

and

G. W. Wilson
Department of Astronomy, University of Massachusetts, Amherst, MA 01003
Received 2004 September 4; accepted 2005 May 18

ABSTRACT

The TopHat experiment was designed to measure the anisotropy in the cosmic microwave background radiation on angular scales from 0.°3 to 30° and the thermal emission from both Galactic and extragalactic dust. The balloon-borne instrument had five spectral bands spanning frequencies from 175 to 630 GHz. The telescope was a compact, 1 m, on-axis Cassegrain telescope designed to scan the sky at a fixed elevation of 78°. The radiometer used cryogenic bolometers coupled to a single feed horn via a dichroic filter system. The observing strategy was intended to efficiently cover a region 48° in diameter centered on the south polar cap with a highly cross-linked and redundant pattern with nearly uniform sky coverage. The Long Duration Balloon flight over Antarctica in 2001 January surveyed about 6% of the sky. Here we describe the design of the instrument and the achieved in-flight performance and provide a brief discussion of the data analysis.

Subject headings: balloons — cosmic microwave background — cosmology: observations — galaxies: general

1. INTRODUCTION

The angular power spectrum of the anisotropy of the cosmic microwave background (CMB) contains information on the physical characteristics of the early universe (Hu & White 1996). Detection of the anisotropy at large angular scales from *COBE* (Bennett et al. 1996) prompted a number of groups to attempt to measure the angular power spectrum on a variety of scales using ground-based, balloon-borne, and satellite platforms. Several groups have designed, built and flown balloon-borne experiments with similar goals in mind. These include the MAX/MAXIMA collaboration (Hanany et al. 1997), the BOOMERANG instrument (Crill et al. 2003), and the Archeops collaboration (Benoit et al. 2002). The results of the *Wilkinson Microwave Anisotropy Probe* (*WMAP*) satellite (Bennett et al. 2003) have confirmed and significantly improved on these earlier measurements.

In this paper we describe the TopHat experiment, an instrument designed to determine the angular power spectrum of the CMB temperature anisotropy on angular scales from 0.°3 to 30° and the thermal emission from Galactic and extragalactic dust. We also discuss the operation of TopHat in flight. The design goals of the instrument and how these drove important features of the instrument are discussed in § 2. Section 3 describes the basic design of the major instrument components and briefly covers the cryogenics system. A detailed discussion of the cryogenic system has previously been published (Fixsen et al. 2001).

Section 4 contains a description of the Antarctic flight, and in-flight instrument performance is compared to the design performance in § 5. In § 6, we briefly discuss the data analysis, calibration, and some measurements of spectra of the LMC and SMC (Aguirre et al. 2003) derived from these data.

2. INSTRUMENT DESIGN CONSIDERATIONS

The high sensitivities achieved by modern CMB experiments are remarkable. However, most of these instruments are equally

[1] Present address: Conceptual Analytics, Glenn Dale, MD 20769.
[2] Present address: Center for Astrophysics and Space Astronomy, University of Colorado, Boulder, CO 80303.

sensitive to the signals of interest and many unwanted radiation sources that may lead to systematic errors. Various systematic errors were of concern in the earliest attempts to detect the CMB from rockets and balloons and still troubled later attempts to measure its anisotropy from all platforms. Some balloon-borne instruments with large beams went to great lengths (literally) to avoid contamination from the balloon and its peripheral equipment by using let-down reels, up ∼2000 feet in length, to relocate the experiment well below the balloon while at the float altitude (Muehlner & Weiss 1973). Even rocket-borne experiments (Matsumoto et al. 1988) were troubled by systematic errors that may have compromised the quality of the data collected.

The design of TopHat was driven by the desire to provide a stable observing platform with an additional level of protection from low levels of systematic errors, especially those resulting from sidelobe contamination. It was also designed to take advantage of the unique characteristics of the Antarctic environment. The principal factors that drove the design for TopHat were (1) control and minimization of systematic errors, (2) high sensitivity and stability, and (3) spectral coverage to allow study of and removal of dust emission in the CMB observation. We discuss these factors below.

2.1. *Control of Systematics*

Control of systematics was a major consideration in designing the TopHat instrument. The major features of the design that attempted to minimize the systematic errors were top-mounting with shielding and the observing strategy.

Mounting the front end of the instrument on top of the balloon allowed for near-zenith observation, minimizing sensitivity to emission from the residual atmosphere, the Earth, and the balloon and its ancillary equipment. This location also made possible TopHat's unique observing strategy. Systematic effects due to far-sidelobe pickup of stray emission—already significantly diminished by mounting the instrument on top of the balloon—were further mitigated by a conical, corotating light baffle that shielded the payload from radiation emitted by Earth and the Sun. This shield is described further in § 3.3.

The experiment used an observing strategy designed to produce a well cross-linked, nearly uniformly observed map of a 48° diameter cap centered on the South Celestial Pole (SCP, see Fig. 1). The high level of cross-linking also allowed for efficient rejection of $1/f$ noise from the final maps. The instrument was mounted on top of a circumpolar long-duration balloon (LDB) launched from McMurdo Station, Antarctica (∼−78° latitude). A generally dependable weather pattern sets up polar vortex winds during the austral summer, carrying an LDB payload around the South Pole at nearly constant latitude, usually taking 10–20 days for a single circumnavigation. TopHat's optical axis was 12° from the rotation axis, and the entire telescope rotated at a constant angular speed with a 16 s period. Assuming constant latitude and a level observing platform, the telescope's beam would intersect the SCP on every rotation, and as the Earth rotated, the center of the beam rotation would move in right ascension while remaining at approximately constant declination. Most regions in the resulting map would be observed from two different approach angles and on a variety of timescales, greatly increasing the ability to distinguish astrophysical signals from those originating in the instrument or from other signals uncorrelated with sky position.

2.2. *Sensitivity and Noise*

In the absence of significant systematic effects, the sensitivity of an instrument is determined by the signal responsivity, system noise, and the efficiency with which incoming radiation is detected. To this end, TopHat used sensitive cryogenic monolithic silicon bolometric detectors with implanted semiconducting thermistors fed by compound parabolic concentrators (CPC), or Winston cones (Welford & Winston 1978), and employed a low-noise readout system for these detectors. Of particular concern in the design of the readout electronics is the noise spectral density between the rotation frequency and about 5 Hz. The rotation frequency is the frequency at which the calibration source of the CMB dipole appeared. The upper frequency, ∼5 Hz, is where the ∼20′ beam size begins to significantly reduce the sky signal power.

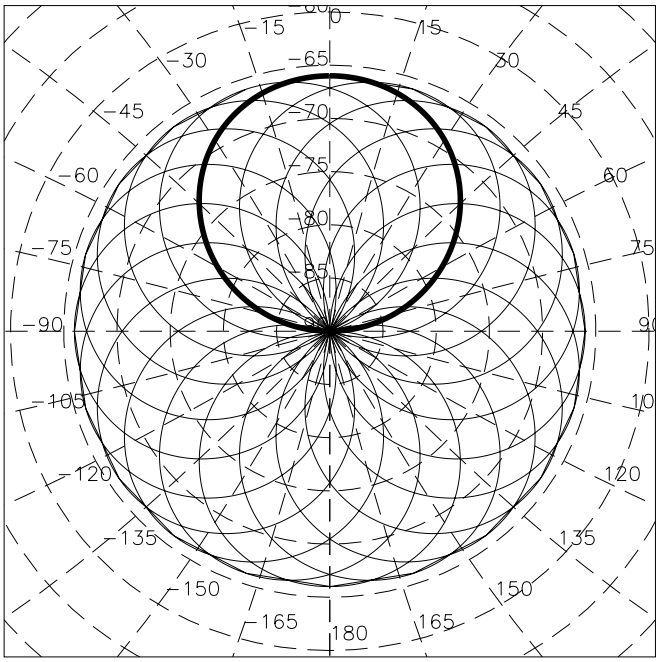

Fig. 1.—Nominal TopHat scan strategy. The scan strategy is illustrated with 20 selected scans spaced evenly over one sidereal day. Coordinates are celestial with R.A. increasing clockwise from the top, and the SCP at the center. A single scan circle (one rotation of the package) is shown in bold.

2.3. *Foreground Removal*

Recent balloon-borne CMB experiments have relied on external foreground templates to demonstrate that diffuse interstellar dust emission is a negligible contamination to their cosmic signal. This method is tenable when the total observing region is small and can be selected for extremely low dust emission. Although the patch of sky TopHat was designed to observe is relatively free of dust, in order to use large, contiguous regions of the sky to determine the CMB power spectrum, it was necessary to perform some kind of foreground removal. Instead of using external templates that rely on extrapolations in spatial or optical frequency, TopHat was designed with three high-frequency channels from which an internal determination of the spatial structure and "color" of the dust emission could be made and removed from the CMB channels.

3. INSTRUMENT DESIGN

The following sections detail how the scientific design goals in § 2 were implemented in the actual instrument.

3.1. *Upper and Lower Gondolas*

The payload was divided into the upper and lower gondolas. The upper gondola was the scientific front-end containing the telescope, radiometer, and front-end electronics mounted on a

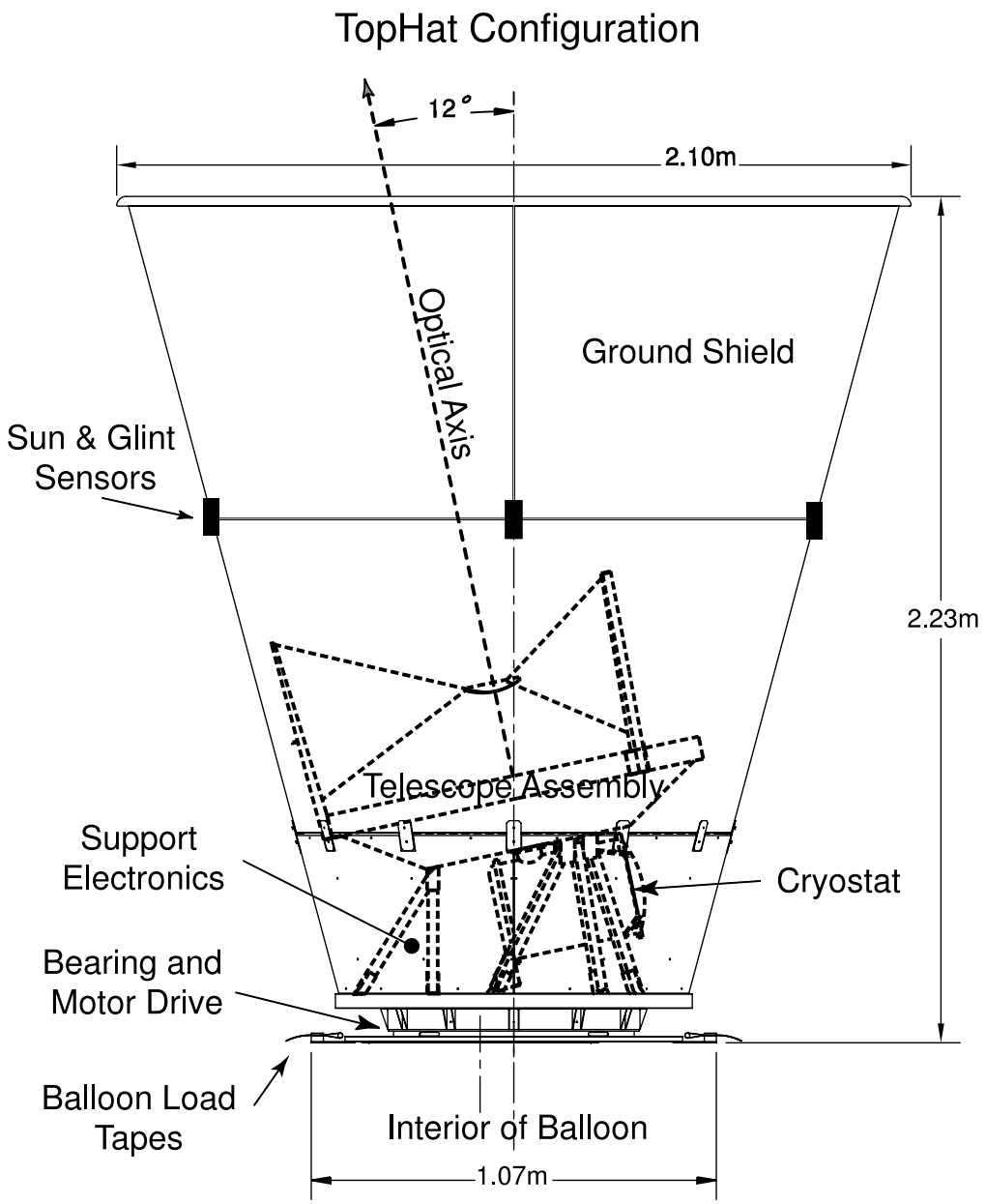

FIG. 2.—Cutaway schematic drawing of TopHat telescope and Sun/Earth shield. The support electronics and a foil shield that surrounds the entire primary mirror are not shown on this diagram. The position of the electronics is indicated, but the electronics are not shown.

plate on the top of the balloon. The lower gondola was suspended in the conventional location below the balloon and consisted of the power system, telemetry and command systems, and on-board computers and storage systems. The gondolas were connected via two sets of redundant communication and power wiring built into the balloon load-bearing tapes.

The major components of the top payload were the telescope, the Sun/Earth shield, the cryostat and radiometer, the readout and communication electronics, the telescope scanning mechanism, a power conversion system, and aspect and attitude sensors to allow reconstruction of the telescope pointing. The design of the upper gondola systems are described in greater detail in §§ 3.2–3.9. A schematic of the upper gondola is shown in Figure 2.

The lower gondola was designed to provide support functions for the upper gondola. It was responsible for power generation and conversion, receiving data from the upper gondola, data storage, data compression for the satellite and line-of-sight (LOS) links, data transmission, and sending commands from the ground to the upper gondola. The lower gondola used commercial electronics housed in a pressure vessel. Power was generated by eight solar panels, backed up by a set of batteries, which supplied power to the upper gondola at 120 VDC. Telemetry and commanding were sent digitally between the upper and lower gondolas with optically isolated transmitters and receivers using the RS-485 protocol. The telemetry and commanding downlink to the ground station during flight was initially an LOS radio link at 16.4 kbps, and switched over to a 3.8 kbps downlink via NASA's Tracking and Data Relay Satellite System (TDRSS) satellite when the balloon went below the horizon. The full, uncompressed data stream was also written redundantly to two 4 Gbyte disks on the lower gondola.

3.2. *Beam Forming Optics*

The 1 m aluminium parabolic primary mirror and a hyperbolic secondary mirror formed an on-axis Cassegrain telescope.

TABLE 1
PRIMARY AND SECONDARY MIRROR PARAMETERS

Parameter	Value (mm)
Prime focal length f	435.2
Primary mirror radius R_p	500.0
Secondary semimajor axis a	175.23
Secondary semiminor axis b	152.96
Secondary mirror radius R_s	66.5
Secondary offset z_0	202.6

The telescope parameters are given in Table 1. The secondary mirror was suspended by kevlar threads tensioned by springs and attached to three legs extending from the edge of the primary. The telescope optical axis was fixed 12° from the nominal local zenith. The cryostat containing the detectors was mounted behind the primary mirror with the effective aperture of the single feed horn at the Cassegrain focus, 30 mm behind the vertex of the primary. The secondary converted the f/0.7 primary feed to f/3.5 at the input horn. The primary and secondary are shown in Figure 2 surrounded by the Sun/Earth shield that protects the entire telescope from direct illumination from the Sun or Earth. The feed horn's field of view was restricted to the secondary mirror and cold sky (rejecting rays from the Sun/Earth shield) by a gold-plated baffle in the shape of a partial CPC attached to the hole in the primary. The feed horn itself consisted of a pair of back-to-back cones with a 14 mm^2 sr^{-1} étendue; the rear horn entering the detector/beam splitter assembly was a CPC, while the forward horn at the cryostat aperture end was a custom-designed nonimaging horn (Fixsen 2001) with a flare at the wide end to reduce diffraction. It minimized radiation originating from outside the radius of the secondary mirror. The angular beam size would be 17′ FWHM if a narrow guard ring on the primary were used, but the flared input horn apodized the beam on the primary leaving a larger guard area and resulting in the expected beam size being ~10% larger. These beams are larger than the diffraction limit at the longest wavelength because some angular resolution was sacrificed for higher sensitivity to the diffuse radiation.

At the predicted resolution and sensitivity of the instrument, existing radio and infrared point source catalogs (e.g., Jaffe et al. 1999) revealed that no sources in the region of the sky accessible to TopHat were expected to be bright enough to be used as a source to map the beam. This necessitated preflight measurements of the beam to constrain its profile.

The critical alignment issue was the position and orientation of the secondary mirror relative to the primary mirror. The other piece of beam-forming optics, the main feed horn, was restricted to move less than ~1 mm with respect to the primary mirror, and the effect of this motion on the beam shape is negligible because of the relatively low optical speed of the system at the horn. At the secondary, the system is quite fast, such that a few millimeters of motion away from the optimal secondary position substantially alters the beam profile. The only mechanism by which the secondary position should change is relaxation of the kevlar threads (tensioned with springs) attaching the secondary to the struts attached to the primary. Kevlar expands as it cools, with a coefficient of thermal expansion, $\Delta L/L = 2 \times 10^{-6}$ K^{-1}, while the aluminium supporting the kevlar contracts by a much larger amount. Measurements were made of the position of the secondary mirror as a function of temperature, and it was determined that the maximum expected motion was 0.1 mm per 20°C temperature change. The beam profile was then measured over a range of secondary positions that conservatively bracketed the range of expected positions in flight.

In June of 1999, the main telescope optics were characterized in the Goddard Electromagnetic Anechoic Chamber (GEMAC) at GSFC. This facility has nonreflecting walls at microwave/far-IR wavelengths and a 3 m off-axis parabolic reflector on one wall. An alt-az mount 12 m from the reflector is used to mount the instrument for test. A chopped source at the facility reflector focus illuminates the primary mirror of the instrument with parallel rays, mimicking a source at infinity. The facility reflector focus is 3.7 m from the reflector near the floor of the chamber. For the 1999 measurement, the instrument optics were mounted on the alt-az stage and configured as a transmitter with a blackbody source placed at the small end of the main feed horn. A 4 K bolometer radiometer was coupled to the focus of the chamber reflector. The beam profile was measured in the various TopHat channels by placing warm bandpass filters in the light path between the reflector focus and the radiometer and rastering the alt-az mount with the TopHat optics. The optimal position of the secondary mirror was determined by making a series of coarse rasters with the secondary in different positions. Fine rasters were taken with the secondary at the optimal position. The measurements were repeated with the secondary up to 3 mm away from the optimal position in either direction along the system optical axis and up to 1 mm away in the two orthogonal dimensions. The measured beam agreed with the design parameters in width and general profile, and the empirically determined optimal secondary position agreed with the design to within 1.6 mm.

Beam determination measurements in the GEMAC were repeated twice, although the second time the blackbody source was placed at the facility reflector focus to illuminate the reflector focus and the TopHat optics operated as the receiver with the flight cryostat and detector system. To assure reproducibility of the secondary position, a jig used to reference the secondary position was used for all further assemblies of the telescope. In June of 2000, the original optical system was measured in this configuration, and in September of 2000, the system was measured with a new secondary mirror designed to produce a smaller beam. Both measurements obtained beams with a steeper than Gaussian profile and a full width at half-maximum of 19′–22′ in the different spectral bands, in close agreement with estimates of the beam size and measurements of the beam out of the cryostat.

3.3. *Sun/Earth Shield*

A conical, corotating aluminum shield surrounds the beam-forming optics, keeping radiation from the Sun, Earth, and balloon surface from the far sidelobes of the telescope beam. The on-axis design of the optics allowed for a simple, compact, lightweight design for this shield, shown in Figure 2. The shield has a double wall with the interior skin thermally isolated from the outside skin to reduce the speed of propagation of temperature changes induced by solar illumination on the outside. Rotating the shield along with the telescope eliminates differential pickup that could result in a scan-synchronous offset in the data. A few days before the flight, when the instrument was in its flight configuration, sidelobe tests were performed. Ground measurements of the far-sidelobe response with the shield in place showed greater than 110 dB rejection beyond 70° from the optical axis and greater than 80 dB between 25° and 70° from the optical axis.

3.4. *Cryostat*

A cryostat with low mass and volume and long hold time was necessary for the top-mounted payload. A custom design was

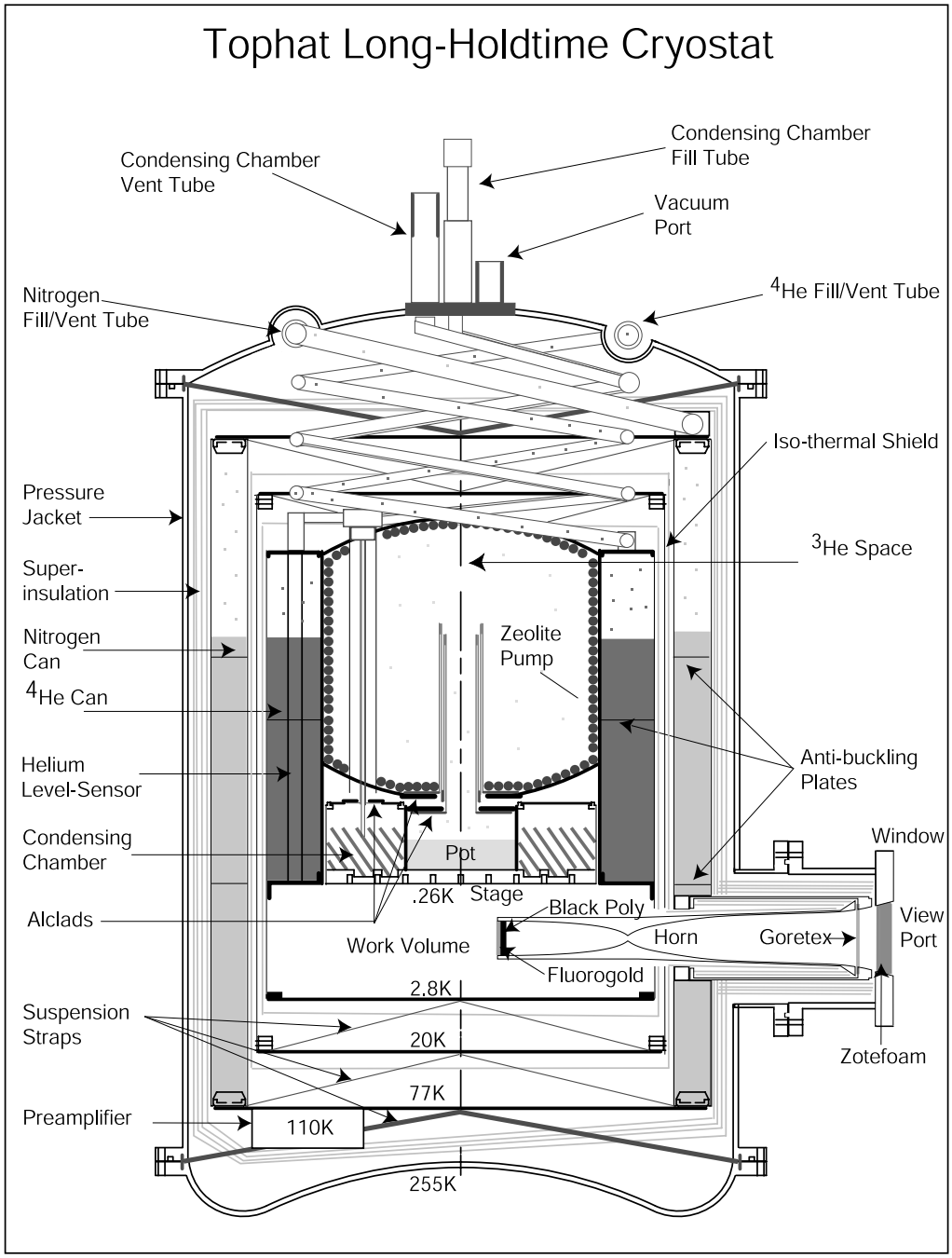

FIG. 3.—Cross section of the TopHat cryostat. Each reservoir was supported by suspension wires to the next layer at the top and bottom. The fill and vent tubes for the nitrogen and helium, and condensing chamber were helical thin-wall stainless steel. At the bottom right was the optical input port with only the 3 K input optics shown.

employed. The cryostat, seen in Figure 3, was an internally pumped ^{3}He refrigerator with supporting liquid ^{4}He and liquid nitrogen (LN2) reservoirs. The cryostat was 35 cm tall and 26 cm in diameter, weighed 10 kg when full of cryogens, and maintained a cold stage temperature of $\sim$260 mK for more than 10 days under simulated float altitude conditions. The small size of the cryostat was in large part due to the development of helical fill tubes that provided a low thermal conduction path in a small physical height.

At the cryostat vacuum window and along the length of the feed horn were filter elements used to block out-of-band radiation and reduce the heat load on the inner cryostat stages. For a complete description of the cryostat design, fabrication, and performance see Fixsen et al. (2001).

3.5. *Radiometer*

The input feed horn was coupled to a five-band dichroic photometer. The two lowest frequency bands are designed to be sensitive to the 2.7 K CMB, while the three highest bands are designed to be sensitive to the thermal emission from interstellar dust grains. A schematic diagram of the radiometer is shown in Figure 4. The expanded end of the output CPC was 16 mm in diameter; this was also the dimension of the photometer input light pipe. The first element an incoming ray encountered in the photometer was a capacitive grid filter (A), which transmitted below 360 GHz and reflected above that frequency. The transmitted ray was further split by a metal-mesh filter (B) that transmitted below 180 GHz and reflected above. The ray reflected

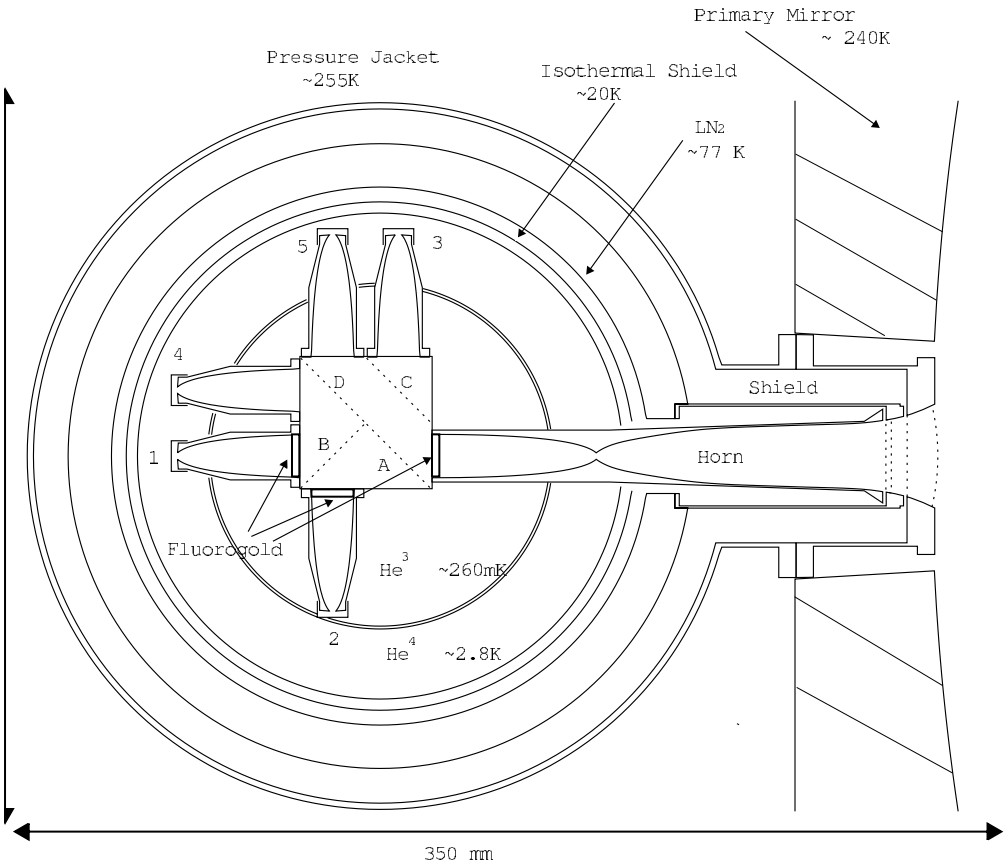

FIG. 4.—Radiometer schematic. The drawing shows the cryostat window and back-to-back input horns at the right that limit the field of view to the secondary mirror and the dichroic assembly. The bolometric detectors are labeled with numbers. Channel 6, the blind channel, is not visible in the figure because it was placed underneath the optics block. The input baffle is not shown on this diagram.

from the first filter passed through two more dichroics, with transition frequencies of 420 GHz (C) and 570 GHz (D). Each of the five resultant beams passed through a final metal-mesh bandpass filter and into a matched CPC terminating in the integrating cavity, which includes a bolometer and backshort. All filters were cross-shaped holes on a metallized sheet. This pattern was made with a lift-off aluminum process on 25 μm mylar. The two lowest-frequency channels had an extra 3 mm section of fluorogold in their CPCs for high-frequency blocking as well as the 3 mm section at the entrance to the optics block. Transmission and reflection spectra of filter elements were measured with a Fourier Transform Spectrometer (FTS). The overall response in each channel of the fully assembled 265 mK photometer was also measured with the FTS. Figure 5 shows room temperature transmission and (if applicable) reflection measurements of individual elements of the filters and beam splitters. Figure 6 shows the measured normalized response for each channel in the fully assembled cold radiometer as a function of frequency. The Rayleigh-Jeans equivalent band centers for the five channels were calculated as

$$\langle \nu \rangle = \left[\frac{\int \nu^2 t(\nu)\, d\nu}{\int t(\nu)\, d\nu} \right]^{1/2} \quad (1)$$

and were 175, 245, 400, 460, and 630 GHz.

3.6. *Detectors*

The TopHat detectors were monolithic silicon bolometers with ion-implanted semiconducting thermistors built at GSFC. Each of the six devices was fabricated on a silicon wafer thinned to 5 μm. The central disk was 2.4 mm in diameter and was supported by four $\sim$30 μm wide legs that provided mechanical support and the thermal connection to the 265 mK bath as well as electrical contacts for the thermistor readout. The in-band absorption of the disk was enhanced by placing a backshort approximately $\lambda/4$ behind the disk and coating the back side of the disk with a thin layer of bismuth. Two thermistors were formed on each disk by ion-implantation doping part of the disk area. Leads from each thermistor to contact pads on the detector frame were formed by degeneratively doping the detector support legs and the paths from the legs to the thermistors.

3.7. *Detector Readout Electronics*

The bolometers were biased by applying a DC voltage generated by a heavily filtered power supply in the warm amplifier to the bolometer in series with a 60 MΩ load resistor. The voltage across each bolometer was coupled to the gate of one of six JFETs (InterFet NJ132L) configured to operate as source followers. The JFETs used in flight were selected for their low voltage noise properties when operating near 77 K. In the selection process the lowest voltage noise was found when operating near 110 K. This operating temperature was attained in the instrument by attaching an aluminum box containing the JFETs to the cryostat LN2 stage, standing the JFETs off from the walls of the box with a fiberglass (G10) tube, and altering the drain current to dissipate the desired amount of power in the JFETs. The JFETs are biased with the same heavily filtered supply used to make the bolometer bias voltage. The JFET preamplifier is discussed in detail by Oh et al. (2001).

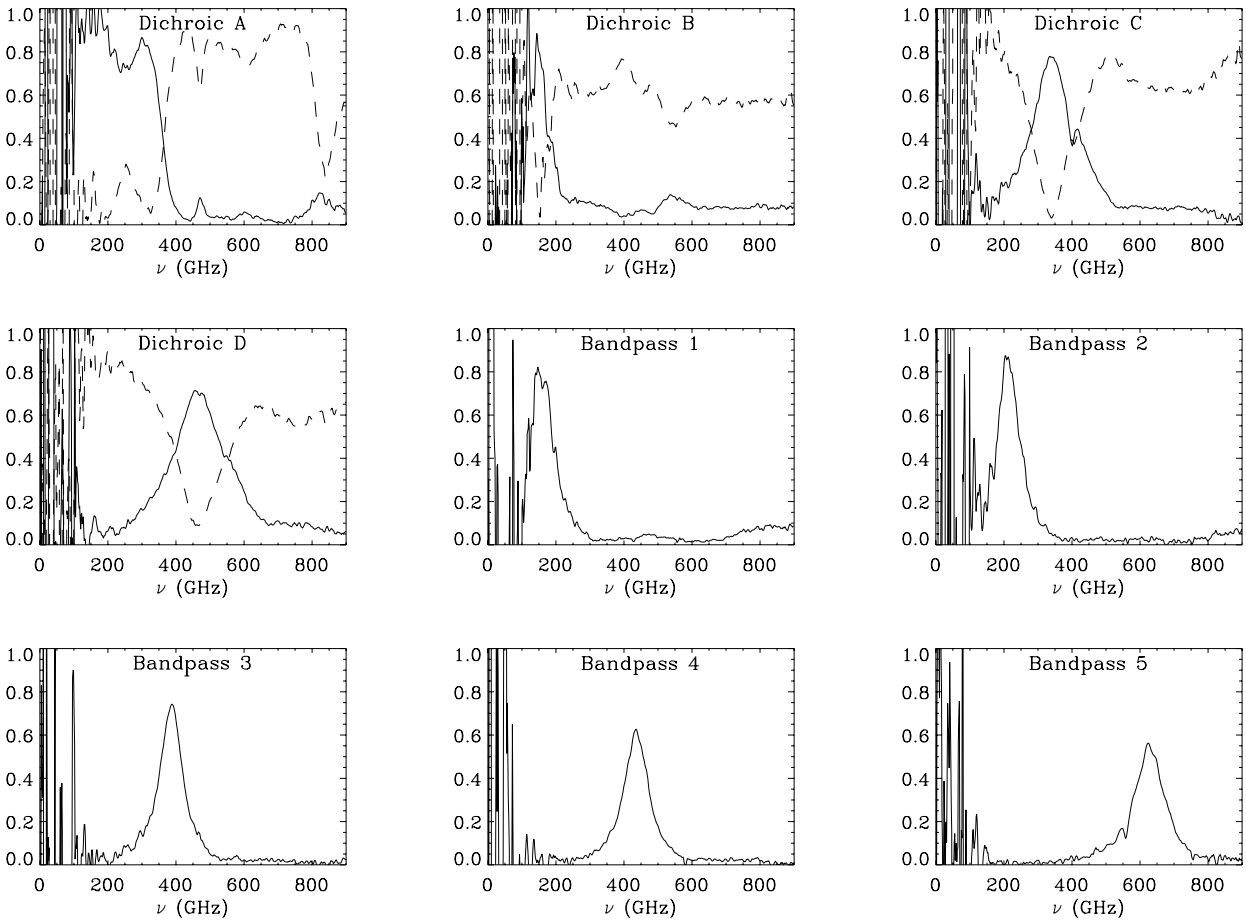

FIG. 5.—Measured transmission (and reflection) vs. frequency for the TopHat photometer individual filter components. In the plots the solid line is transmission, and the dashed line is reflection (for the dichroic beam splitters).

The output signal from the JFET was fed to the input of a warm amplifier and also through an operational amplifier buffer into the signal chain to measure the DC voltage for load curves. The warm amplifier circuits had two high-pass stages with cutoff frequencies at approximately 0.1 Hz and a low-pass filter with a cutoff around 600 Hz. The warm amplifier output was fed to a 22-bit sigma-delta analog-to-digital converter with a sinc^3 internal digital filter with its first zero at 128 Hz. The output of this device was packed into the telemetry stream after convolution with an acausal 16 Hz low-pass digital filter that was down 50 dB by 32 Hz.

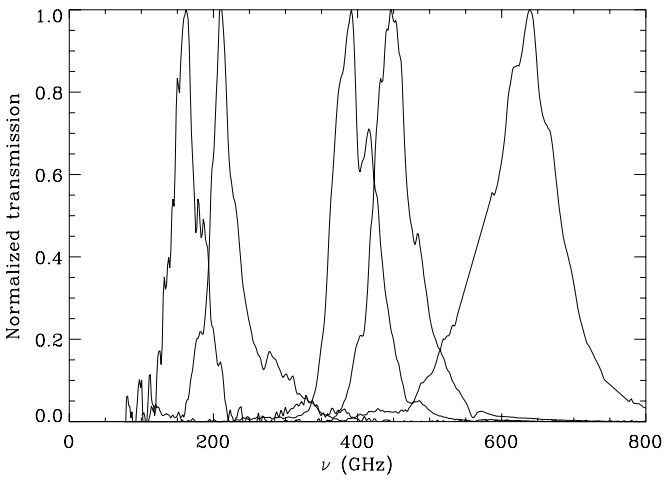

FIG. 6.—Measured transmission of fully assembled, cold photometer. Peak response in each channel has been normalized to 1.0.

The warm amplifier box and cryostat were mechanically coupled via a split-ring collar around the electrical connector. This collar was tightly clamped during operation, effectively making the cryostat and amplifier a single Faraday cage. The electrical connections from the amplifier to the rest of the readout electronics were made through EMI-filtering connectors and the entire amplifier had a dedicated analog power supply and its own ground path. All high-impedance wiring in the cryostat (i.e., all wiring up to the JFET preamp) is secured to the body of the cryostat or optics block. The total noise contribution from the warm amplifier and JFET preamp (referred to the input of the source follower) was measured to be less than 10 $\mathrm{nV}/\sqrt{\mathrm{Hz}}$ above 1 Hz and less than 50 $\mathrm{nV}/\sqrt{\mathrm{Hz}}$ down to the spin frequency of 1/16 Hz. Figure 7 shows a block diagram of the signal electronics. Noise properties of the electronics are reported by Oh et al. (2001).

3.8. *Pointing Sensors*

TopHat was designed to be operated by spinning the instrument at a constant angular velocity relative to the balloon and then using attitude sensors to reconstruct the in-flight pointing. The parameters of the attitude system were determined from data taken on the ground before the flight, although in-flight verification was possible. The sensors included a two-axis tiltmeter, two-axis gyroscope, and custom-made coarse and fine Sun sensors.

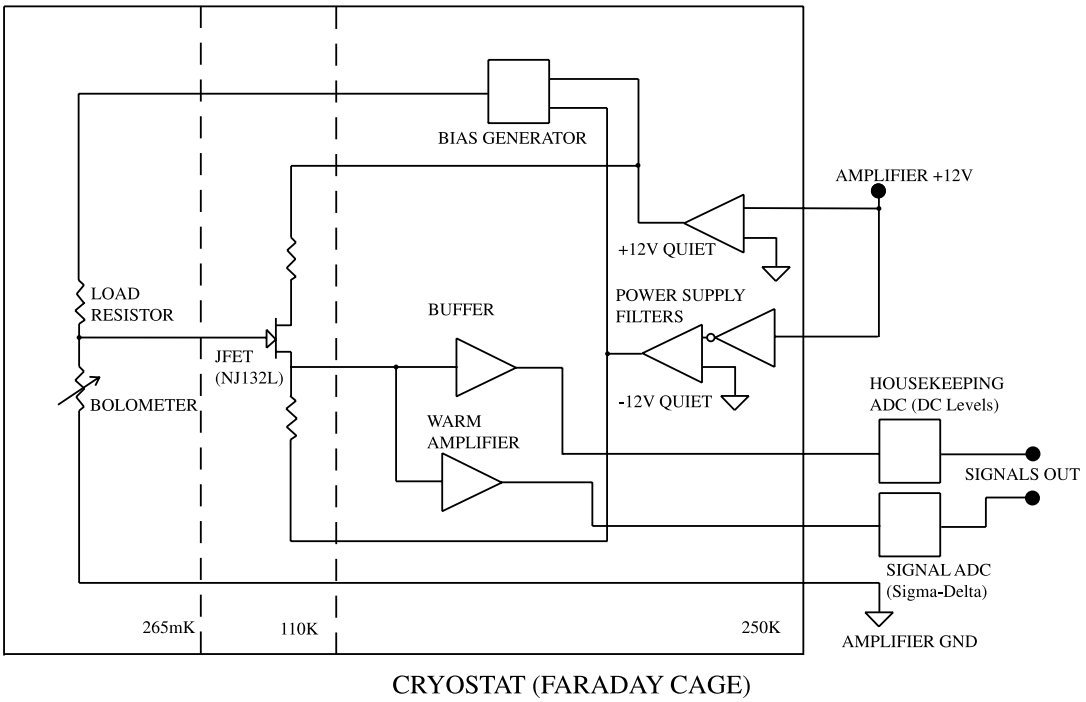

FIG. 7.—Schematic of the TopHat bolometer readout electronics. The Warm Amplifier reads out the ac-coupled signal while the Buffer is directly coupled to the input FET.

In a nominal TopHat flight the platform on top of the balloon on which the instrument was mounted would be nearly horizontal throughout the flight. The telescope spin axis would always be near the local zenith (determined from GPS information), and determination of where the instrument beam pointed would require only two other pieces of information: the angle between the beam and the spin axis (nominally 12°) and the azimuth of the beam relative to a line between the spin axis and some fixed point in the sky such as the Sun. Under the further assumption that the telescope rotated at constant angular velocity and that the balloon as a whole rotated much more slowly than the telescope, this second angle need only be measured at a low frequency and interpolated to the detector sampling rate.

The necessary pointing parameters were intended to be measured with four Sun sensors mounted on brackets $\sim 90^\circ$ apart on the outside of the shield approximately 75 cm from the top of the shield. The actual angular separations were determined by measurement before flight and were verified in flight. Each sensor consisted of a coarse Sun sensor and a glint sensor—a small telescope that imaged the Sun onto a photodiode through a mask. Each coarse sensor was simply a solar cell whose response to the Sun was (ideally) proportional to the cosine of the angle between the Sun and the normal to the solar cell surface. The glint sensor imaged the Sun through an N-shaped mask. Only the timing of the center glint was necessary for the nominal flight. The time of the glints was recorded with 1/8000 s precision. The field of view of the glint sensors was 35° between 2°.5 and 37°.5 elevation. It overlapped with but was not identical to the Sun sensor field of view, in part because of a baffle installed beneath the sensors to guard against reflections from the balloon and the ground.

To convert the signal from either set of Sun sensors to the azimuth of the beam with respect to the Sun, it was necessary to know the relative azimuth of the boresight of each Sun sensor to the telescope beam. These angles were measured on the ground before the flight by setting the top package spinning and observing the Sun. Relative offsets of the sensors were confirmed in flight. A single azimuth parameter was fitted by allowing the angle of one sensor to be a free parameter in the pointing model fit for the telescope beam (see § 5.4 for a description of this process).

3.9. *Rotation System*

The drive system seen in Figure 2 was designed to rotate the entire platform on which the telescope was mounted at a constant rate of one rotation every 16 s. Electrical connection between the rotating platform and the baseplate and lower gondola was accomplished through a 36-channel slip ring. The rotation system had to provide uniform motion over a wide range of temperatures to avoid injecting microphonically induced noise into the detectors. To achieve this, the telescope platform was connected to the baseplate via a high-precision, large-diameter (25″.5) Kaydon bearing. The platform was rotated by a stepper motor with a small pulley turning a large pulley via a toothed kevlar timing belt. To provide smoother rotation, the stepper motor was driven with an analog sine-wave current rather than the more energy efficient square wave drive; in this system, the angular position of the drive shaft was proportional to the frequency of the driving waveform. Via command, the rotation direction could be reversed. There was no feedback between the rotation system and the pointing sensors. This drive system provided the ability to change direction, apply torque, and generate the required rotation speed with little mechanical complexity. The performance of the drive system during flight is discussed in § 5.5.

3.10. *Thermal Design*

Both the top-mounted instrument and the support gondola were painted with Goddard white, a low optical absorption,

high-emissivity (in the thermal infrared) paint to reduce external heat input by reflecting incident optical radiation and efficiently radiating to the ambient environment. The solar panels on the bottom gondola were not mounted normal to the average solar elevation but instead were mounted at 20° from horizontal to avoid overheating at altitude. This configuration was not optimal for power conversion, but sacrificed solar panel efficiency for a simple passive thermal design. The only active thermal control on the lower gondola was the use of internal fans to regulate the temperature of the support electronics and on-board data storage disks in the pressurized vessel.

The thermal requirements on the top payload were more complicated. The electronics were designed to remain within operational bounds without requiring convective cooling while exposed to the ambient environment at float altitude. The outer shell of the cryostat needed to be kept as cold as practical because it was the dominant source of heat load on the LN2 in the cryostat. A thermostatically controlled heater was attached to the cryostat shell to prevent it from freezing its O-rings.

Two main design features were motivated by the desire to have the optics and cryostat run as cold as possible. The cryostat and optics were thermally isolated from the electronics and the rest of the rotating deck by means of a jacket made from aluminized mylar and fiberglass insulation. In addition, the aluminum primary mirror (infrared emissivity $\sim$0.05) was coated with a thin layer of silicon dioxide (infrared emissivity $\sim$0.75) to increase its infrared emissivity and allow it to dump heat radiatively to the cold sky. Because of their non-negligible in-band emissivity, the telescope optics were designed to be as cold as possible with this passive cooling to reduce the optical load on the detectors.

A thermal model mock-up of the top package was constructed and tested in two test flights. Relatively high temperatures were recorded in the mock electronics in one of the test flights, and the problem was remedied by employing a passive conductive cooling system in which the flight electronics were thermally coupled to Thermacore heat pipes (1/4 inch copper tubing partially filled with either water or methanol, depending on the operating temperature range) that transported heat to a series of panels around the perimeter of the lower portion of the top package (below the Sun/Earth shield). The exterior of these panels was coated with silver Teflon tape for good IR emissivity without sacrificing optical reflectivity. In the Antarctic flight the electronics temperatures ran between -20°C and 40°C, well within the acceptable range.

4. GENERAL DESCRIPTION OF THE FLIGHT

4.1. *General Overview*

After a nominal launch from Williams Field at McMurdo Station on 2001 January 4, the following activities were carried out before data-gathering operations began: (1) during ascent the package was set to turning and the optimal motor torque setting was established by observing the detector noise level over a range of motor drive settings; (2) later in the ascent the optimal threshold setting for the glint sensor trigger was established and set; (3) once TopHat had reached float altitude, a load curve was taken for each detector and analyzed to determine the optimal bias voltage setting under the flight operating conditions. A short time was spent observing the detector time streams to establish the optimal gain setting.

After detector gains and biases were set, TopHat entered observing mode. This continued until one sidereal day later, at which time load curves were taken and analyzed again; both the polarity of the bias voltage and the telescope rotation direction were reversed as a check on systematic errors. The telescope then reentered observing mode and remained there for another sidereal day. At the end of the second sidereal day the bias polarity was reversed again. From this time the telescope was in observing mode continuously until the cryogens were exhausted.

All telescope systems performed nominally during the course of the Antarctic flight. The bearing and motor drive turned the telescope without slippage at the nominal preflight torque level. All components of the telescope ran at temperatures within expected limits. In flight, the primary mirror varied in temperature between 225 and 255 K, while the cryostat exterior varied between 245 and 265 K. The electronics and on-board sensors performed as expected. The telemetry stream was recorded by the on-board disk drives on the bottom gondola. This on-board stream was uninterrupted except for short periods totaling less than 10 s over the entire flight.

The LOS link was fully operational during the time the balloon was visible above the horizon, for the first 1.2 days of flight. The TDRSS link functioned at nearly 100% for the first day of flight and rapidly degraded thereafter. The problem was later traced to a failing TDRSS uplink transmitter on the balloon. Fortunately, the data disks were eventually recovered, so the loss of the TDRSS link only affected our ability to send commands. Some systematic controls, e.g., reversing detector bias and reversing rotation direction, could not be carried out after the early part of the second day.

4.2. *Anomalous Tilt of Observing Platform*

The platform on top of the balloon on which TopHat was mounted was designed to be horizontal. In North American test flights with similar, but not identical balloons, less than 1° of tilt was observed. However, during most of the Antarctic LDB flight this platform was tilted from horizontal by about 5°. The observed tilt of the platform on top of the balloon was a strong function of altitude near float altitude (see Fig. 8). Until the balloon reached $\sim$15 km, the tilt angle was less than 1°. At float altitude the tilt angle varied diurnally as the balloon altitude varied. When converted to an estimated balloon radius using a spherical balloon model, this observed behavior was consistent with a linear dependence of estimated balloon radius with tilt angle.

The most plausible theory we have generated for the cause of this tilt is a load imbalance on the balloon caused by the wiring embedded in the side of the balloon for power and communication to the top package. Two sets of redundant wires were embedded into load tapes along two different balloon seams. Although the request was that these wires be embedded on opposite sides of the balloon, a review of the as-built configuration worksheet showed that the cables had been placed in two bundles on adjacent gores of the balloon. The total mass of the balloon wiring was approximately 35 kg. In the toy model in which this entire mass hangs off the side of a rigid sphere and is balanced with the gondola weight hung off the bottom of the sphere, the tilt induced is about 2° [$\theta_{\rm tilt} = \tan^{-1}(M_{\rm wiring}/M_{\rm gondola})$], which is of the right order of magnitude.

This model also predicts the observed behavior of the tilt angle as a function of tension in the material making up the skin of the balloon and, hence, the balloon altitude. As the balloon rises (falls) it becomes more (less) fully inflated, and the surface tension in the balloon material increases (decreases). The greater the surface tension, the farther the wiring will be held from the

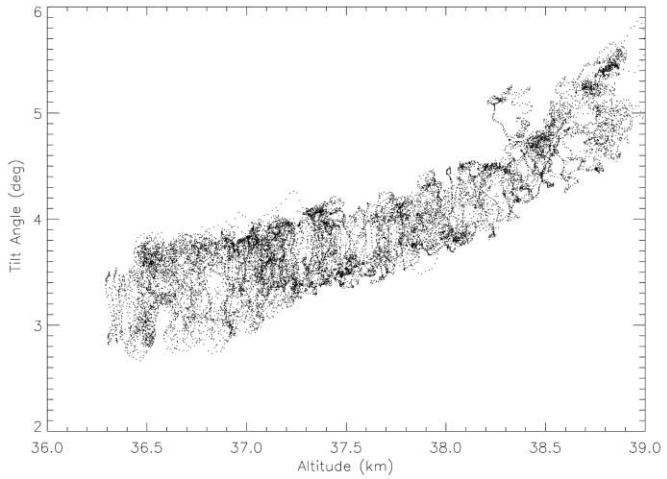

FIG. 8.—Tilt angle of the TopHat spin axis vs. altitude at float altitude.

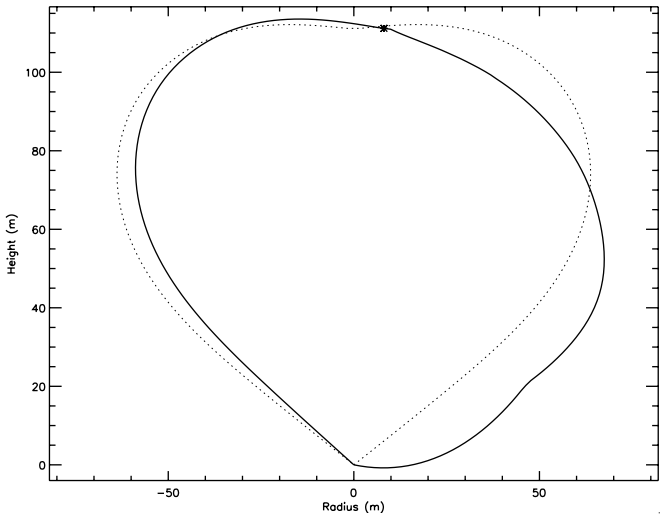

FIG. 9.—Calculated balloon shape. The figure shows the nominal balloon shape (*dotted line*) and the estimated abnormal shape (*solid line*) in a section through the gore containing the extra balloon wiring. The asterisk (*) shows the location of the top payload on the abnormal balloon shape curve.

center of mass, thereby exerting more torque on the instrument platform. Also, the greater the surface tension the greater the restoring force of the balloon material on the side of the instrument platform that is opposite the wires. Both of these effects cause the tilt angle to be positively correlated with balloon altitude.

To more accurately account for the effect of the wiring, a three-dimensional deformable model of the balloon was constructed. The model included the detailed shape of the 159 gores and the mass of the plastic in each gore as a function of distance from the bottom of the balloon to the top. The balloon was a modified standard 29 million cubic foot balloon, the same as in the TopHat Antarctic launch. Some details of the balloon are shown in Table 2. The shape of the balloon that results is shown in Figure 9. The model shows that the helium moves to the opposite side of the balloon from the wires, exaggerating the imbalance. The net tilt is then $\sim 5^\circ$, in good agreement with the measured value. The $\sim$200 kg of telescope and other gear on top of the balloon has little effect other than to depress the platform on top of the balloon by $\sim$0.8 m. Both the model and the measurements in flight showed that once the balloon had reached its final shape it would be very stable and dynamic effects (rotation, winds, etc.) would change the tilt by only about 2 mrad ($0\overset{\circ}{.}1$). The change of tilt with altitude (see Fig. 8) is more difficult to model but preliminary results show the same scale of change, about 1° km^{-1} of altitude change.

TABLE 2
BALLOON PARAMETERS

Parameter	Value
Weight	1790 kg
Volume	834500 m^3
Length	180.6 m
Maximum gore width	2.56 m
Number gores	159
Number caps	3
Balloon thickness	20 μm
Surface area	44000 m^2
Top weight	195 kg
Suspended weight	900 kg
Cable 1 location	Gore 158
Cable 1	16 16 ga Cu wires
Cable 2 location	Gore 159
Cable 2	8 twisted pair

The primary effects of the tilt on the science goals of the instrument are discussed in §§ 5.4 and 5.5.

5. COMPARISON OF FLIGHT TO DESIGNED PERFORMANCE

5.1. *The Instrument Beam*

As discussed in § 3.2, there were no bright point sources expected in the region scanned by TopHat nor in the larger region actually observed. As such, an alternate method for determining the in-flight beam was necessary. To attempt to verify the in-flight beam, we have used the spatial characteristics of some regions that were previously studied at nearby wavelengths.

Galactic dust emission was detected in the four highest-frequency TopHat channels with high signal-to-noise, and certain predictions are made about the spatial distribution of this dust that can be used to infer the in-flight beam. Finkbeiner et al. (1999, hereafter FDS99) have constructed a model of high-latitude dust emission in the microwave by extrapolating DIRBE-corrected *IRAS* data using a color index derived from DIRBE 100 and 240 μm data and fitted at the low-frequency end to the FIRAS measurements. This model has spatial information down to the *IRAS* resolution of $5'$. Though the resolution of the DIRBE-based color index map is only $0\overset{\circ}{.}7$, if it is assumed that the dominant factor in the small-scale variation in emission is dust column depth and not temperature or spectral index, the predictions of this model can be used as a spatial template with which to compare the TopHat measurements of high-latitude dust emission. We take five regions of high dust emission (shown in Fig. 10) and fit measurements of emission in these regions to the predictions of the FDS99 model convolved with Gaussians of various widths. Figure 11 shows the reduced χ^2 of this fit in channels 2 through 5 as a function of the size of the kernel used to smooth the FDS99 prediction. Due to the large number of degrees of freedom ($\sim$2000) in this fit the observed reduced χ^2 indicates very poor agreement with the model. Individual fits to the smaller dust regions are significantly better, possibly indicating that our noise model is poor at large angular scales.

What is clear, however, from the results of this fit is that in every channel, the FDS99 model smoothed by a $45'$ Gaussian

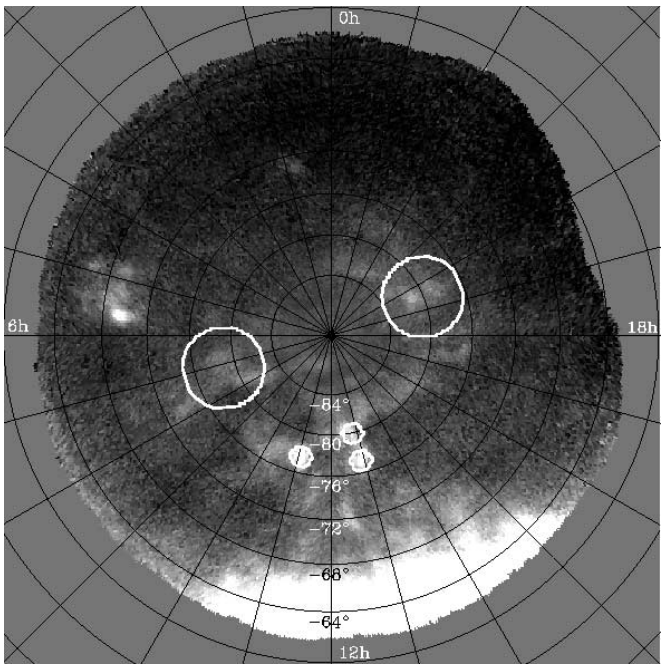

FIG. 10.—Regions used in fit to FDS99 model.

was a significantly better fit than FDS99 smoothed by a 20′ Gaussian. It is possible that the morphology of Galactic dust emission changes significantly over the factor of 5 in frequency between the 3000 GHz *IRAS* data used in the FDS99 model and the highest TopHat channel. If this were the case, one might expect the best-fit smoothing of FDS99 in Figure 11 to exhibit frequency dependence within the TopHat bands; it does not, but this does not rule out the possibility of a fundamental difference in spatial behavior between the dust at 3000 GHz and the dust in our bands. A result that has been fairly consistent across a large frequency range is the power-law behavior of the angular power spectrum of Galactic structure. The Galactic emission has a spatial power spectrum described by a power law $C_l \propto l^{-\beta}$ with $\beta \sim 3.0$ in the infrared (Gautier et al. 1992; Wright 1998), radio (Crovisier & Dickey 1983), and microwave (Masi et al. 2001) regions of the spectrum. Figure 12 shows angular power spectra of the TopHat 400, 460, and 630 GHz channels for a region covering the inner 10° radius about the SCP. A map was constructed using the inner 6000 pixels of the full HEALPix[3] $N_{\rm side} = 256$ maps. These spectra are then fitted to a model consisting of a power law in l times the l-space window function of a Gaussian beam. The dashed lines show the best-fit model with no constraints on power-law index or width of the Gaussian beam, while the dotted line shows the best fit attainable assuming a 20′ beam. The degree to which this result depends on the fidelity of the noise model is shown in the fourth panel of Figure 12, in which the power spectrum of the 630 GHz channel

[3] Available at http://www.eso.org/science/healpix.

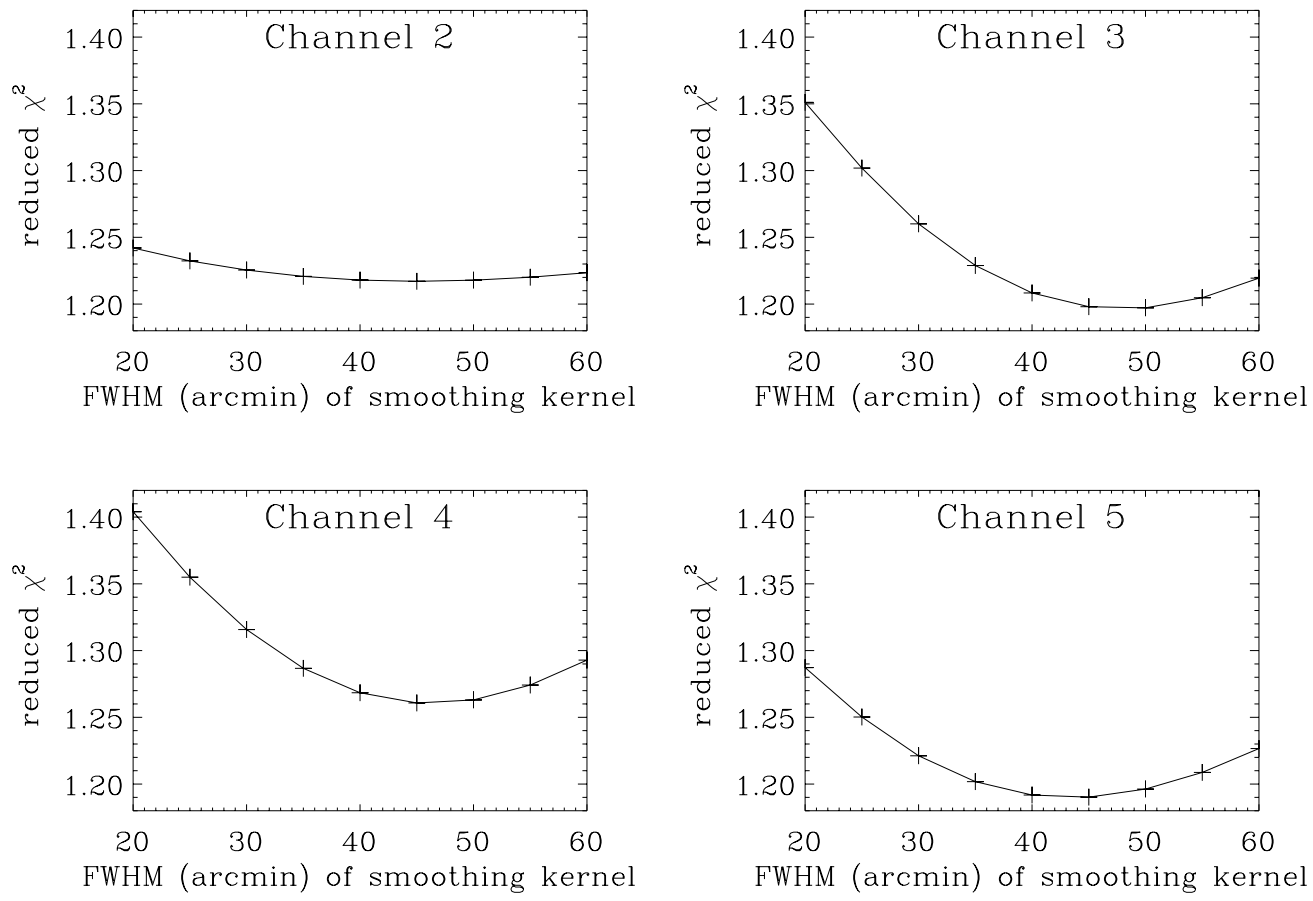

FIG. 11.—χ^2 of fit of five dusty regions to smoothed versions of FDS99 model.

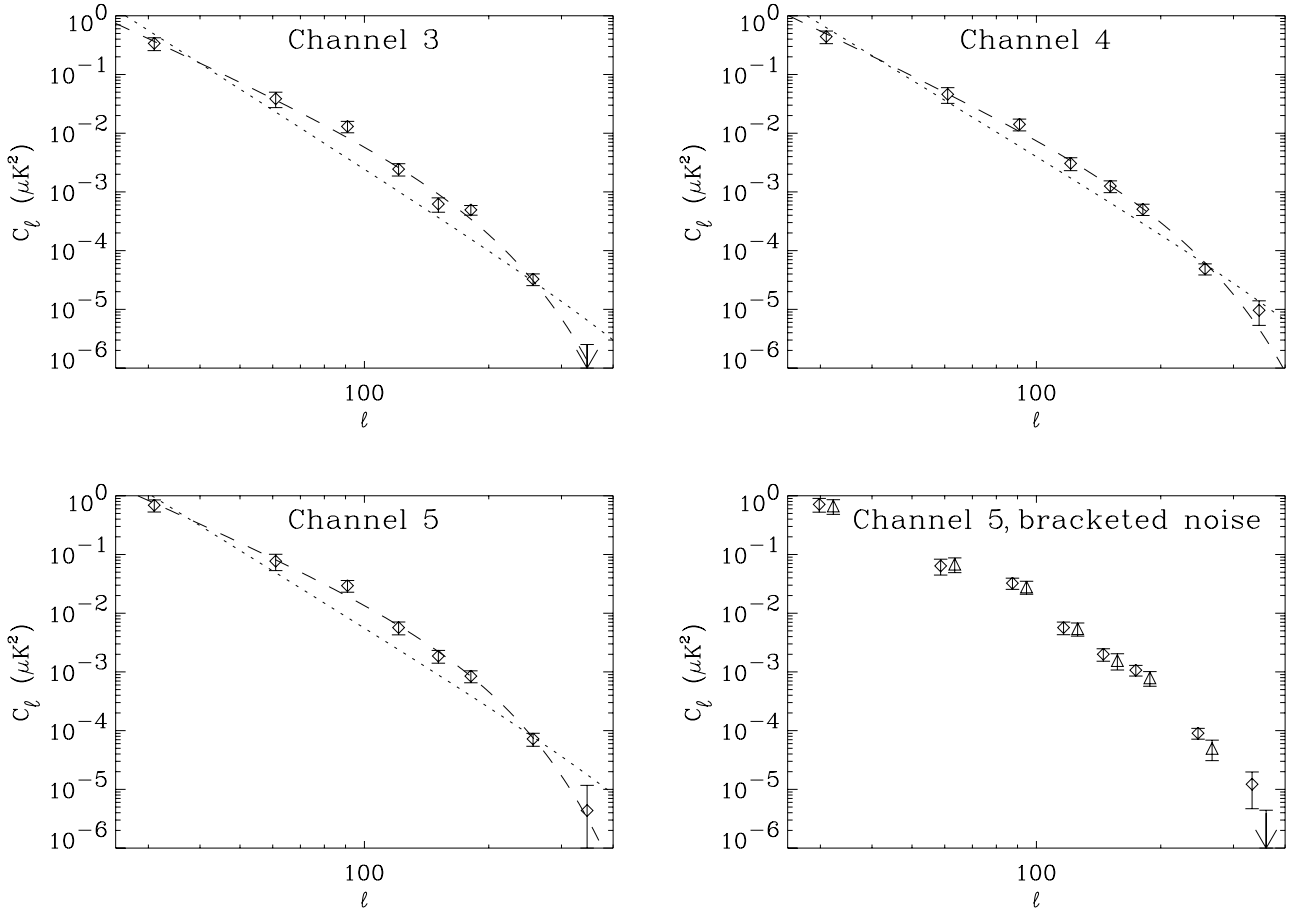

FIG. 12.—Power spectra of three highest-frequency channels.

is shown assuming two different extremes of the noise model—one in which none of the power at the harmonics of the rotation frequency is considered to be noise and one in which the noise model is constructed by interpolating between the residual power at the rotation harmonics. Best-fit beam sizes and power-law indices and the associated χ^2 are summarized in Table 3.

These two comparisons leave us with no evidence that the TopHat in-flight beam was the same as preflight ground measurements and some evidence that it was significantly larger in flight than preflight. In Appendix A, we describe alignment sensitivities and discuss some possible causes for the large beam size during flight. In all cases, these causes appear unlikely due to the large displacements from the nominal positions required to produce the observed performance.

The safest approach we can take is to put an upper bound on the beam size from the smallest source observed in our maps. Figure 13 shows two cuts through the channel 5 image of the star-forming region 30 Doradus in the Large Magellanic Cloud (LMC) (pixelized at HEALPix $N_{\rm side} = 512$, pixels $\sim 7'$ on a side). The shape of this source is very similar in the other channels as well. If we assume that the width of the source is entirely due to the TopHat beam, we infer a beam full width at half-maximum (FWHM) of close to 1°.

TABLE 3
χ^2 AND PARAMETERS FOR BEST FITS TO DUST POWER SPECTRA

Channel	Beam FWHM (arcmin)	β	χ^2 per d.o.f.	PTE
3.....	72	3.24	1.7	0.13
4.....	62	3.36	0.8	0.54
5.....	73	3.12	0.6	0.69

5.2. *Cryostat*

The cryostat performed within expectations given the loading conditions observed just before launch. The limiting factor in cryostat hold time is the main ^{4}He stage, and an elevated boil-off rate was observed before launch that implied approximately a week of flight-condition hold time. About one day of that was lost in the 12 hours spent on the ground between the last ^{4}He fill and launch, which should have left about six days at float. In fact, the cryostat warmed up about 4.5 days after launch. This discrepancy could be within the uncertainty in the hold time estimate, but it could have also been negatively affected by flight conditions discussed in § 4.

5.3. *Detectors*

The five detectors viewing the sky performed nearly as expected, but the 175 GHz channel exhibited some excess noise properties, even on the ground. This additional noise in combination with the consequences of the unexpectedly large tilt of the top platform rendered the 175 GHz channel only marginally useful.

The rate of cosmic-ray hits on the TopHat bolometers was approximately 2 per minute. The hits were detectable above the time stream noise, and the rate was $\sim$50% larger than the rate experienced by the BOOMERANG collaboration (Crill et al. 2003) with detectors specifically designed to reduce cosmic-ray

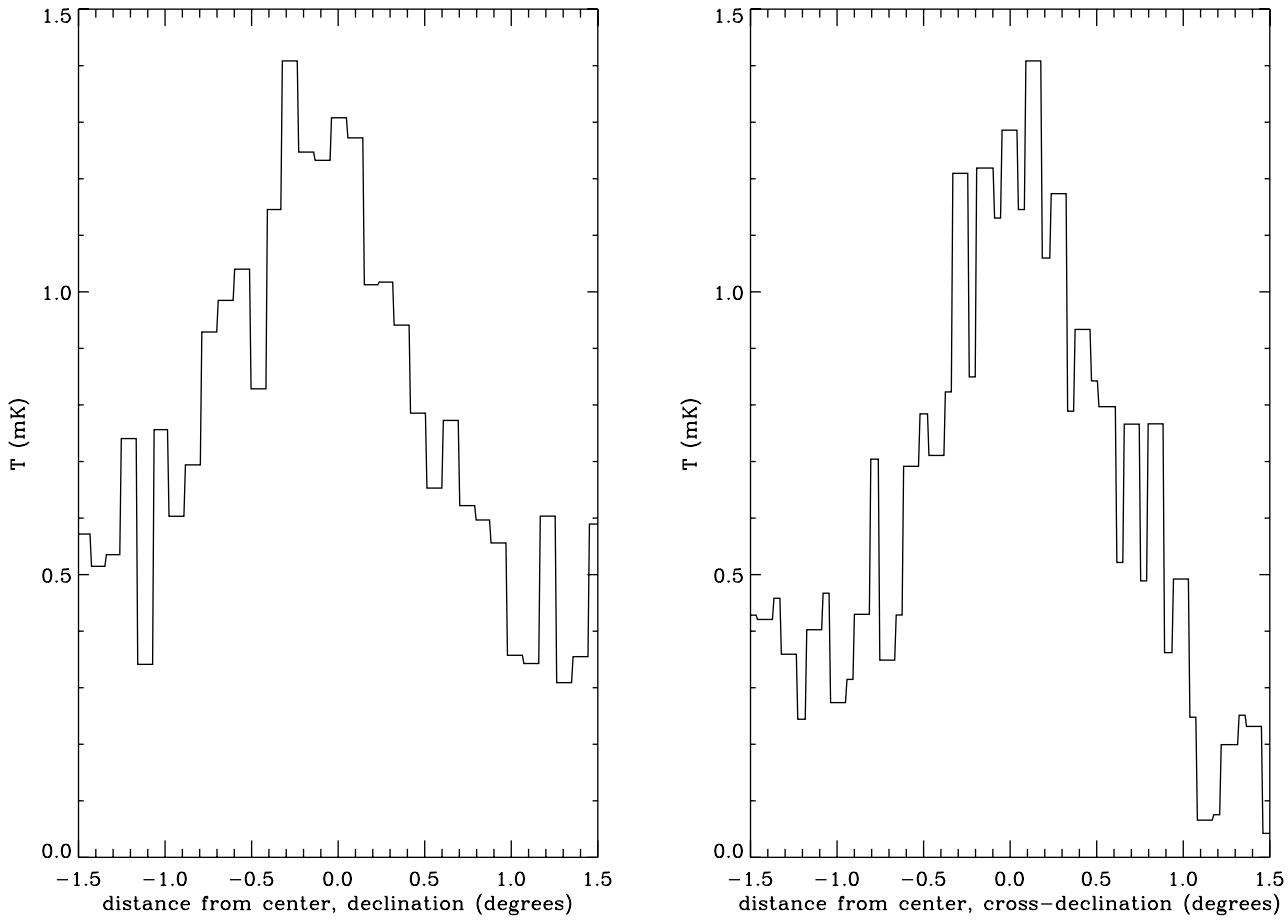

FIG. 13.—Orthogonal cuts through the channel 5 image of 30 Doradus.

cross section. These events were well fitted by a model of a delta-function power deposition on the bolometer so only a few data samples were lost for each cosmic-ray hit. The resultant data loss from cosmic-ray hits was only ∼0.1%.

The characteristics of the bolometers as determined from the in-flight load curves are summarized in Table 4. This table shows the estimated optical loading, $P_{\rm load}$, the measured bolometer time constants, $\tau_{\rm eff}$, and the theoretical performance, $\rm NET_{RJ}$ and $\rm NET_{CMB}$, in the absence of any systematic effects. The predicted voltage noise spectral density for some of the channels is shown in Figure 14 together with noise spectra obtained from flight data. The predicted noise budget at ∼2.5 Hz and the total ∼2.5 Hz noise measured in flight are summarized for each channel in Table 5.

5.4. *Tilt and the Pointing Sensors*

Under the assumption that the TopHat mounting platform was nearly horizontal, that the telescope rotated uniformly throughout the flight, and that the balloon rotated slowly compared to the rotation rate of the telescope, the in-flight pointing of the telescope beam could be determined completely using slowly sampled azimuth data from the Sun sensors. While the last two criteria were satisfied in flight, the first was strongly violated. As a result of the anomalous instrument platform tilt, it

TABLE 4
DETECTOR PARAMETERS AND CHARACTERISTICS IN FLIGHT

Parameter	Ch. 1	Ch. 2	Ch. 3	Ch. 4	Ch. 5	Ch. 6	Units
$\nu_{\rm cen}$	175	245	400	460	630	(Dark)	GHz
C(0.27 K)	10.0	9.95	12.3	7.9	6.6	4.8	pJ $\rm K^{-1}$
$V_{\rm bias}$	77	103	180	155	206	51	mV
$R_{\rm bolo}$	38.5	22.2	8.1	11.0	9.1	129	$M\Omega$
$T_{\rm bolo}$	319	343	432	430	443	265	mK
$\tau_{\rm eff}$	23.0	12.0	7.5	9.6	18.3	50.1	ms
$P_{\rm load}$	14	25	103	101	689	∼0	pW
S	−334	−247	−100	−118	−118	−953	MV $\rm W^{-1}$
$\rm NET_{RJ}$	205	96	98	90	110	NA	$\mu\rm K\ \sqrt{s}$
$\rm NET_{CMB}$	451	389	2210	4250	45200	NA	$\mu\rm K\ \sqrt{s}$

NOTE.—The quantity $\tau_{\rm eff}$ is the effective time constant inferred from the 3 dB point.

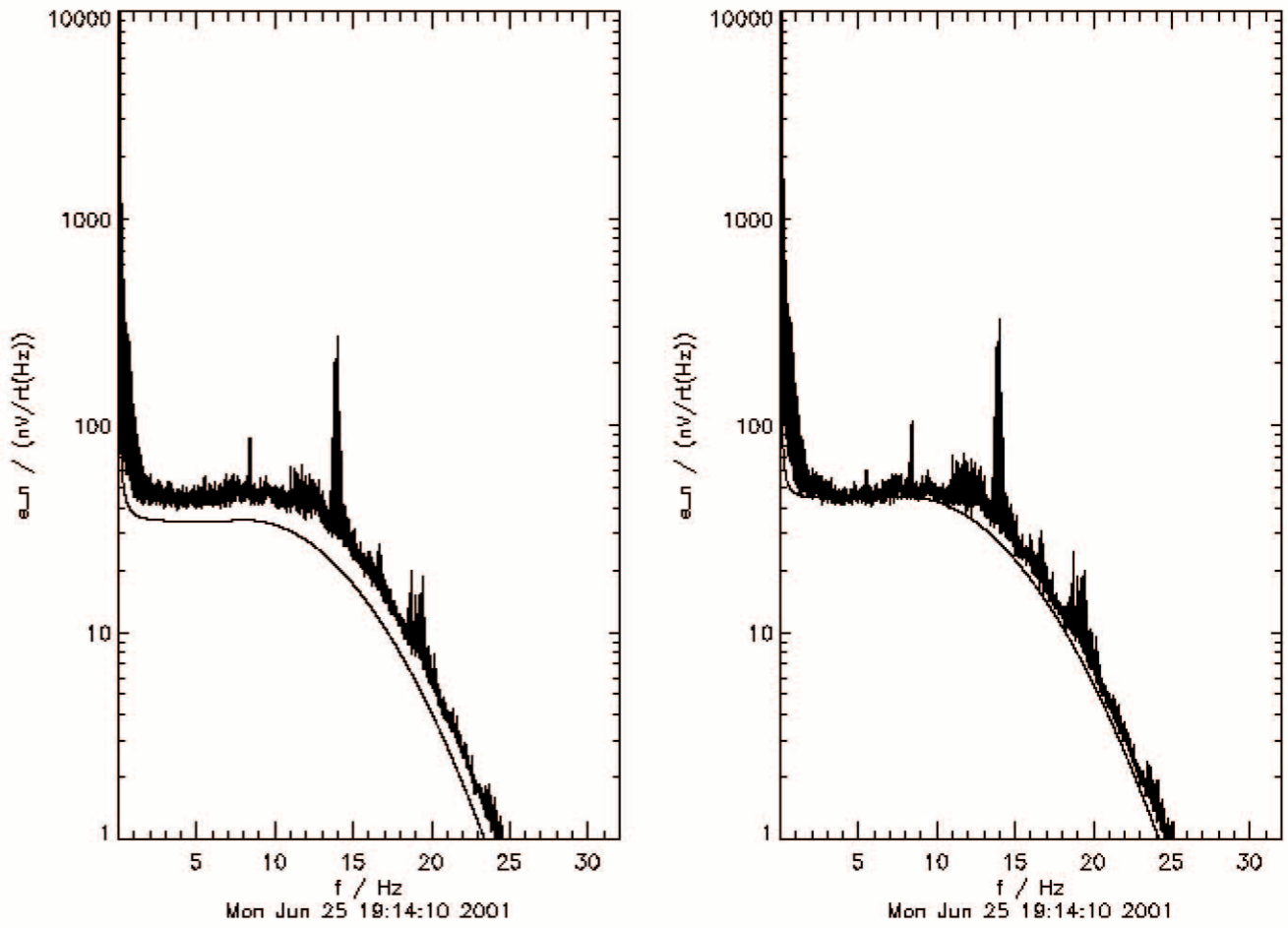

FIG. 14.—Measured vs. predicted voltage noise spectra in the 400 and 460 GHz channels. Both the predicted and measured spectra are shown after the system transfer function has been deconvolved—a rolloff of the high-frequency part of the deconvolution filter is responsible for the 16 Hz low-pass seen in these plots.

became necessary to reconstruct the pointing direction of the telescope spin axis in flight, since the assumption that it would always point near the local zenith was not true. Despite this added complication, the combination of azimuth measurements from either Sun sensor and the elevation information in the data from the tiltmeter, gyroscope, or glint sensor provided enough information to solve for the complete attitude for most of the flight. The methods used to recover the telescope attitude are discussed in Appendix B.

5.5. *Systematic Effects*

A few kinds of instrumental effects were evident in the data, most due to the anomalous tilt. The most serious effect was a large spin-synchronous signal at the rotation frequency. There were also signals at harmonics of the spin frequency whose phase was not locked to the rotation. There was both broadband and line contamination from the rotation system. And finally, the anomalous tilt of the telescope sometimes caused the Sun to reach elevations in the telescope frame that were higher than those for which the Sun/Earth shield was designed, thus contaminating $\sim$1% of the data. These data were discarded and were not used in further analysis.

A plausible physical model for the spin-synchronous signal is that it was due to the internal optics of the cryostat moving with respect to the cryostat shell as the tilted telescope rotated, thus chopping the horn beam slightly between the hot optics and the cold sky. To first order, this effect would be expected to be proportional to the tilt amplitude and mirror temperature, and most of its power would reside in the first harmonic of the rotation frequency, phase locked to the rotation. A model with these features was tried and it removed a large portion of the spin-synchronous signal, but left a residual with significant structure at the first harmonic, implying that the model was reasonable, but that additional features were present in the data that were unmodeled. One of these may be a signal due to modulation of varying atmospheric column depth, since we no longer

TABLE 5
NOISE BUDGET AT $\sim$2.5 HZ FOR SIX TOPHAT CHANNELS

Noise	Ch. 1	Ch. 2	Ch. 3	Ch. 4	Ch. 5	Ch. 6	Units
Photon	19	30	24	33	34	0	nV/$\sqrt{\text{Hz}}$
Detector	38	33	28	32	32	37	nV/$\sqrt{\text{Hz}}$
Total (predicted)	43	45	38	47	47	37	nV/$\sqrt{\text{Hz}}$
Total (measured)	110	55	45	45	35	100	nV/$\sqrt{\text{Hz}}$

observed at constant elevation, though this is highly degenerate with the larger spin-synchronous signal. No particularly compelling physical model was evolved for the higher harmonics; these were modeled as sine waves with slowly varying amplitude and phase.

The vibration noise spectrum of the rotation system was dominated primarily by lines at the motor shaft rotation frequency and its sidebands, and by uneven stresses in the bearing as it rotated in its housing. This vibration spectrum appeared in the bolometer time streams. Because the motor shaft frequency was commensurate with the rotation frequency, the lines induced by the drive could be removed without affecting the astrophysical signal. The bearing noise was evidenced both as broadband blue noise correlated with the dark bolometer and by temporally localized "pops," corresponding to sharp spikes in the time stream. The broadband noise was removed by correlation analysis and the "pops" by flagging with the same algorithm used to detect cosmic-ray strikes. The detector noise associated with the rotation did not appear to be a function of the tilt angle.

The spin-synchronous signals at the rotation frequency and its harmonics, where the astrophysical signal was present, were the dominant limitation to the sensitivity that could be achieved by TopHat. Due to their large size, removal of these undesirable noncelestial signals required a very accurate model. Unfortunately, the models described above were incapable of eliminating the residual contamination due to these systematic effects at the $\sim 10^{-3}$ level required for CMB anisotropy work.

6. DISCUSSION AND CONCLUSIONS

We have described the TopHat experimental hardware and in-flight performance during its LDB flight from McMurdo Station, Antarctica in 2001 January. Most systems performed nominally; however, an unexpected large tilt ($\sim 5^\circ$) at the mounting point of the top payload caused substantial scan-synchronous instrumental signals, which significantly compromised the quality of the CMB anisotropy data. In addition, there is evidence for a larger beam size than we had measured prior to the flight. Nevertheless, due to the large sky coverage and the sensitivity achieved, some interesting dust features can be studied.

In the most general terms, our maps of the SCP region out to $\delta \sim -60^\circ$ are the first such images produced of this part of the sky in these frequency bands at degree-scale angular resolution. Taking into consideration the potential contamination in the long-wavelength spatial modes in our maps, the most immediately accessible non-CMB science to be gained from the TopHat data would seem to be measurements of the flux from extended discrete sources. The uncertainty on the beam shape (see § 3.2) limits the angular resolution with which we can make such measurements, but there are many bright sources with appropriate angular extent in our maps—including the Large and Small Magellanic Clouds (LMC and SMC), the Chameleon Nebulae, and some sources in the Galactic plane—for which we can calculate the integrated flux in a region large compared to the upper limit on the TopHat beam size. The particular strategy used to make these measurements is motivated by the differential nature of the instrument and the types of systematic errors to which TopHat is most susceptible. To obtain spectral information for these sources, a calibration for the higher frequency channels is required. We have used the Chameleon Nebulae and other high-latitude Galactic sources for this calibration and used the results to present calibrated spectra of the LMC and SMC—including separate measurements of the active star-forming region 30 Doradus (the Tarantula Nebula) in the LMC (Aguirre et al. 2003).

We wish to thank NASA's Research Opportunities in Space Science initiative under the Astronomy and Physics Research and Analysis program for support in the development, flights, and data analysis phases of this effort under NASA grant NAG5-11443. We also thank the crews and staff of the National Scientific Balloon Facility, Goddard Space Flight Center, and Danish Space Research Institute for their extensive support in the development of hardware and procedures to permit our modest efforts to extend the capabilities of balloon-borne packages to come to fruition. Special thanks to Joe Novello and Peter Kenny for their extensive and sustained efforts. We also wish to thank Lyman Page, for his contribution in the early portion of the development of the TopHat payload.

Some of the results in this paper have been derived using the HEALPix package (Górski et al. 1999).

APPENDIX A

BEAM SIZE

Below we consider some possible reasons for the substantially larger beam size we observed during the TopHat flight as compared to our ground measurements. None of these scenarios appear plausible in light of the substantial dimensional changes required and the preflight testing done. Others are inconsistent with the measurements in flight.

Misaligned on the ground.—Is it possible that the TopHat telescope was misaligned on the ground? The ground alignment was not done with a far field source, but with the GEMAC where a source is placed at the focus of a reflector to simulate a source at infinity. Had the source been misplaced and TopHat was aligned to this source, then the TopHat telescope would be misaligned for an astronomical source.

This appears unlikely because the GEMAC facility has been used by many instruments that were aligned there and later found to be properly aligned. In our case, an estimate of the misplacement of the GEMAC source required to produce the focus error we observed is about 30 cm. Although possible, this is an unreasonably large error.

Displacement of the secondary mirror.—The most obvious choice for a focusing error is that the secondary mirror was displaced after launch. Because of the secondary suspension system design, only motion of the secondary along the axis of the telescope is likely and other optical components would have to move nearly impossible distances to account for the observed beam size. Breakage of a single kevlar fiber in the secondary suspension would have resulted in the secondary falling onto the primary, so only an extremely wide beam (the beam out of the cryostat) would have resulted in that case.

A more likely scenario might be displacement of the secondary along the primary telescope axis due to thermal effects. In such a case, the displacement would be symmetric due to the design of the secondary suspension system. The optics are fastest at the secondary, so small displacements could have major effects on the beam shape and size. Since we were keenly aware of this possibility, some calculations

and tests of the mirror and secondary suspension had been done prior to the TopHat flight. Secondary position sensitivity was estimated at ± 1 mm for measurable changes in beam size. To grow as large as the observed beam, a 3 mm displacement was required.

To test these calculations, the assembled telescope was cooled from room temperature to -20°C in a large test chamber at the University of Chicago and the change in secondary position was monitored. The secondary mirror suspension worked as planned, compensating for the negative coefficient of thermal expansion of the kevlar. The observed displacement of the secondary was only 0.3 mm, well within the range expected for insignificant beam size changes.

Failure of the secondary mirror suspension.—Another possible failure was that one (or more) of the secondary suspension kevlar fibers had broken after launch. However, due to the way the secondary was suspended, an outright breakage of a kevlar suspension fiber would have resulted in the secondary mirror being removed from primary beam with the result that the instrument could not have functioned as well as it did.

A slippage of a suspension fiber could have displaced the secondary. However, only if such slippage were symmetric would the mirror have moved only along the telescope axis. A axial displacement is required to explain the opening angle of the scan cone, which was observed to be near the nominal opening angle (measured at $11\overset{\circ}{.}9$ compared to the planned 12° angle).

APPENDIX B

POINTING RECONSTRUCTION

The actual pointing reconstruction algorithm used for TopHat employed the glint sensor and tiltmeter data only, except during times when the glint sensors could not see the Sun, in which case the coarse Sun sensors were used. The angles between the axes of these various sensors and the beam were measured before the flight, but to ensure both accuracy and precision, they were included as free parameters in a fit of the time stream data to a map. The beam pointing was uniquely determined by the sensor data and these angles, so these angles were varied in order to minimize the χ^2 of the fit and so obtain best-fit values and uncertainties—uncertainties that were propagated through the pointing model to determine the formal uncertainty on the beam location.

The algorithm used in reconstructing the beam R.A. and declination from the pointing sensor data was a two-step process. First, the location of the spin axis relative to the Sun and local zenith was determined. Then the location of the beam relative to the spin axis and the local zenith was determined. The geometry involved consisted of four spherical triangles as shown in Figure 15. The vertices of the triangles are the Sun, the telescope spin axis, the telescope beam center, the local zenith, and the "effective zenith." The effective zenith points opposite the apparent direction of the local gravity vector in the balloon's frame of reference. For a balloon moving at constant velocity above the Earth's surface, the zenith and effective zenith are coincident. For a balloon that is accelerating (e.g., due to wind shear), the acceleration causes a change in the tilt-meter data resulting in the effective zenith being offset from the local zenith. Inclusion of this effect improved the pointing model, on average, by a few arcminutes. The overall rms pointing error after determination of the free parameters was about $8'$.

In addition to complicating the pointing reconstruction algorithm, the tilted platform also broke the fundamental symmetry of the observing strategy, introducing a new degree of freedom: the angle between the side of the balloon toward which the instrument tilts and the SCP. If this angle had been 90° throughout the flight, then the beam would have intersected the SCP on every rotation, and the observing pattern would have been essentially unchanged from the planned pattern. However, if the instrument rotation axis had been tilted further toward or away from the SCP, the beam would have either missed the outer edge of the desired map and overobserved the area near the SCP

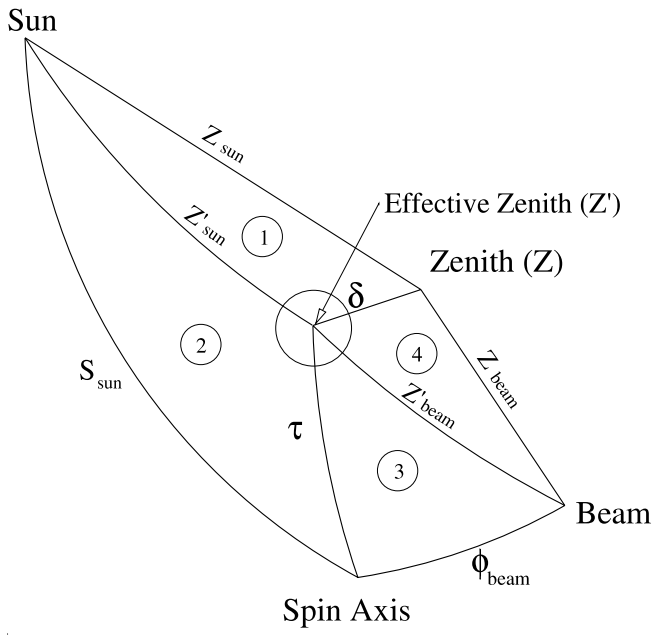

FIG. 15.—Geometry of pointing reconstruction algorithm. The sides and angles for the four spherical triangles (*labeled by numbered circles*) are solved to recover the R. A. and declination of the telescope beam.

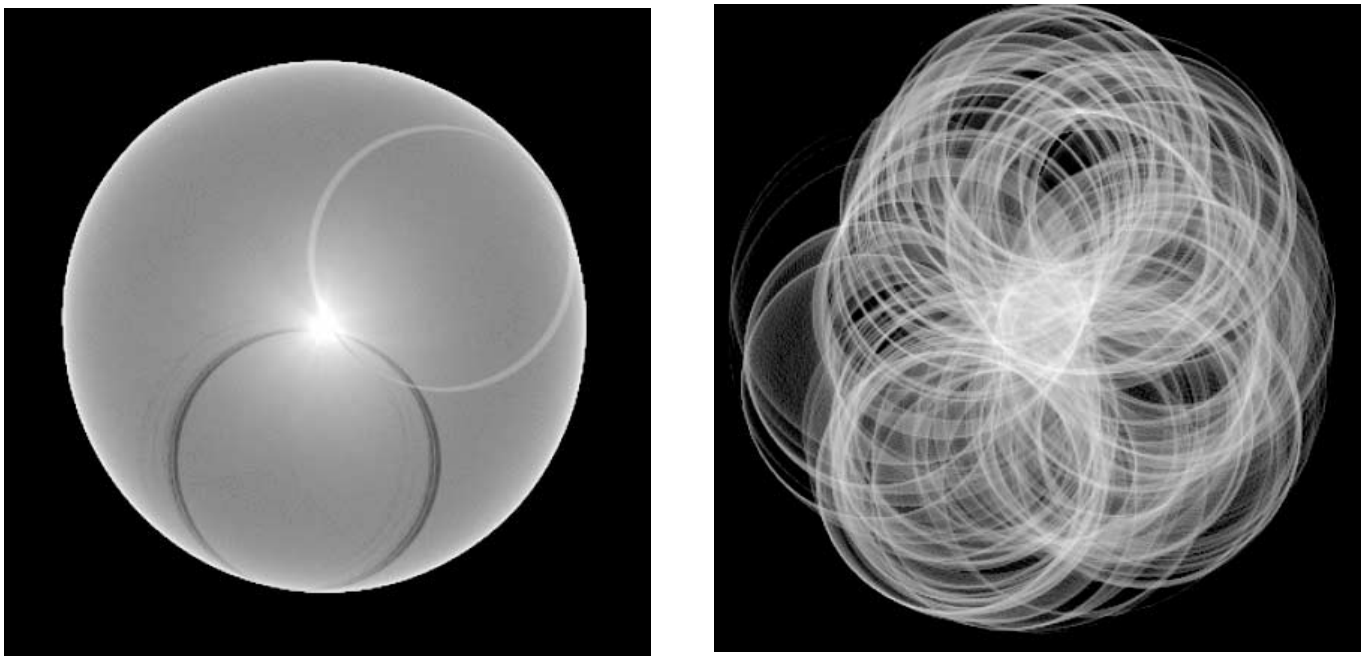

FIG. 16.—Day 1 sky coverage with and without tilt. The SCP is at the center of each figure and each square is 30° on a side. The bright ring on the left of the figure is due to slight overlap of the data in the first day due to motion along the balloon's trajectory. The dark ring is due to telemetry dropouts.

or missed the area near the SCP and extended the outer edge of the map. Since the balloon rotated throughout the flight, all of these conditions were met at some time, and the resulting observing pattern was some combination of these scenarios. Figure 16 shows two maps of sky coverage from the first sidereal day of TopHat observations. The first map shows what the coverage would have been had the top platform been level—with all other variables as they were in flight—and the second shows the actual first day coverage. The unintended tilt resulted in a significantly larger total area covered (6% of the sky as opposed to the planned 4%) including some coverage in the Galactic plane. The high signal-to-noise observations of this part of the sky were crucial in the actual reconstruction of the beam attitude (see § 5.1).

REFERENCES

Aguirre, J. E., et al. 2003, ApJ, 596, 273
Bennett, C. L., et al. 1996, ApJ, 464, L1
———. 2003, ApJ, 583, 1
Benoit, A., et al. 2002, Astropart. Phys., 101
Crill, B. P., et al. 2003, ApJS, 148, 527
Crovisier, J., & Dickey, J. M. 1983, A&A, 122, 282
Finkbeiner, D. P., Davis, M., & Schlegel, D. J. 1999, ApJ, 524, 867 (FDS99)
Fixsen, D. J. 2001, Proc. SPIE, 4446, 161
Fixsen, D. J., Cheng, E. S., Crawford, T. M., Meyer, S. S., Wilson, G. W., Oh, E. S., & Sharp, E. H. 2001, Rev. Sci. Instrum., 72, 3112
Gautier, T. N., Boulanger, F., Perault, M., & Puget, J. L. 1992, AJ, 103, 1313
Górski, K. M., Hivon, E., & Wandelt, B. D. 1999, in Evolution of Large Scale Structure: From Recombination to Garching, ed. A. J. Banday, R. K. Sheth, & L. N. da Costa (Garching: ESO), 37
Hanany, S., et al. 1997, in Microwave Background Anistropies, ed. F. R. Bouchet, R. Gispert, B. Guiderdoni, & J. Tran Thanh Van (Gif-sur-Yvette: Editions Frontiéres), 143
Hu, W., & White, M. 1996, ApJ, 471, 30
Jaffe, A. H., et al. 1999, in ASP Conf. Ser. 181, Microwave Foregrounds, ed. A. de Oliveira-Costa & M. Tegmark (San Francisco: ASP), 367
Masi, S., et al. 2001, ApJ, 553, L93
Matsumoto, T., et al. 1988, ApJ, 329, 567
Muehlner, D., & Weiss, R. 1973, Phys. Rev. D, 7, 326
Oh, E. S., Sharp, E. H., Fixsen, D. J., Cheng, E. S., Inman, C. A., & Silver, C. 2001, Rev. Sci. Instrum., 72, 2735
Welford, W. T., & Winston, R. 1978, The Optics of Nonimaging Concentrators—Light and Solar Energy (New York: Academic Press)
Wright, E. L. 1998, ApJ, 496, 1